ELSEVIER

Journal of Fluids and Structures 19 (2004) 621–634

JOURNAL OF FLUIDS AND STRUCTURES

www.elsevier.nl/locate/jnlabr/yjfls

Transient response study on rolling effectiveness of multiple control surfaces

D. Tang, A. Li, E.H. Dowell*

Department of Mechanical Engineering, and Materials Science, Duke University, Durham, P.O. Box 90300, Durham, NC 27708-0300, USA

Received 8 September 2003; accepted 26 January 2004

Abstract

A study of the effectiveness of trailing- and leading-edge control surfaces has been made for a rolling wing-fuselage model. An experimental model and wind tunnel test are used to assess the theoretical results. The theoretical model includes the inherently nonlinear dry friction damping moment that is present between the spindle support and the experimental aeroelastic wing model. The roll trim equation of motion and the appropriate aeroelastic equations are solved for different combinations of leading- and trailing-edge control surface rotations using a reduced-order aerodynamic model based upon the fluid eigenmodes of three-dimensional vortex lattice aerodynamic theory. The focus is on the transient response of the system. The present paper provides new insights into the transient dynamic behavior and design of an adaptive aeroelastic wing using trailing- and leading-edge control surfaces.

1. Introduction

Some interesting results reported from the active flexible wing (AFW) program by Noll and Eastep (1995) and more recent by Andersen et al. (1997), Zink et al. (1998), Weisshaar et al. (2000), Flick and Love (1999) and Yurkovich (1995) on active aeroelastic wing (AAW) technology have shown that an appropriately chosen combination of leading- and trailing-edge control surface deflections plus an adaptive control law can be used to achieve improved rolling performance and/or to minimize roll maneuver loads. As reported previously by Dowell et al. (2003) and Tang et al. (2003), the same conceptual benefit that can be obtained by using an adaptive torsional stiffness change can also be realized by using an adaptive aeroelastic wing with the gearing ratio between leading- and trailing-edge control surfaces programmed to change with flight dynamic pressure. Also some new actuation technologies are currently under development for high-bandwidth actuators, leveraging high-energy density materials such as piezoceramics. Two such actuation technologies include the X-frame actuators developed at MIT, see Prechtl and Hall (1999) and the V-stack actuator developed at Duke University see Ardilean and Clark (2001). Thus, implementation of an adaptive aeroelastic wing with leading- and trailing-edge control surfaces appears promising.

Dowell et al. (2003) considered theoretically the basic adaptive concept and the fundamental physical phenomena for two models, (i) an airfoil and (ii) a rolling wing. The theoretical results have been validated by subsequent experimental work by Tang et al. (2003). In Tang et al. (2003), a wind tunnel wing-fuselage model with leading- and trailing-edge control surfaces has been designed and tested to measure the steady state rolling effectiveness versus flow velocity for

*Corresponding author. Tel.: +1-919-660-5302; fax: +1-919-660-0089.
E-mail address: dowell@ee.duke.edu (E.H. Dowell).

0889-9746/$ - see front matter © 2004 Published by Elsevier Ltd.
doi:10.1016/j.jfluidstructs.2004.01.006

Nomenclature

A, B	vortex lattice aerodynamic coefficient matrices
c	wing chord (including the leading and trailing control surface chords)
I_α, I_ϕ	torsional and rolling inertias, respectively
l	wing span
L	lift distribution on the wing
M_d	Coulomb friction damping moment coefficient
M_y	total aerodynamic moment about the elastic axis
km, kn	numbers of vortex elements on wing in x-, y-directions, respectively
kmm	total number of vortices on both the wing and wake in the x-direction
K_{ij}	aerodynamic kernel function for the horseshoe vortex
K_α	torsional stiffness of the wing
p	rolling rate
p_s	static or steady state rolling rate
r	$\equiv \eta_{le}/\eta_{te}$
r_f	radius of the slender body (fuselage)
R_a	degrees of freedom of reduced-order aerodynamic model
t	time
T	transfer matrix from the downwash on the local vortex lattice mesh on the wing to the global vortex lattice mesh
U	airspeed
x, y	streamwise and spanwise coordinates
X, Y	right and left eigenvector matrices of vortex lattice eigenvalue model
x_{ja}, x_{jb}	x-positions of the two jth trailing vortex segments
y_{ja}, y_{jb}	y-positions of the two jth trailing vortex segments
Z	eigenvalue matrix of vortex lattice aerodynamic model
α	twist angle of the wing
Γ	vortex strength
Δp	pressure distribution on the wing
Δt	time step, $\Delta x/U$
Δx	$\equiv c/km$
η_{le}	rotational angle of leading edge (positive up) control surface
η_{te}	rotational angle of trailing edge (positive down) control surface
ξ	damping coefficient
ρ_∞	air density
ϕ	rolling angle
$(\dot{})$	$\mathrm{d}(\ )/\mathrm{d}t$

different combinations of leading- and trailing-edge control surface rotation. Time marching simulation has been used to compute the steady state rolling performance, but the experimental/theoretical study was essentially for static equilibrium conditions. A three-dimensional incompressible (linear) vortex lattice aerodynamic theory and a corresponding reduced-order aerodynamic model was used in Tang et al. (2001, 2003) and in the present analysis, see Dowell and Hall (2001). Steady state results for subsonic, compressible flow can be obtained using the Prandtl–Glauert scaling law. It is noted that for the wind tunnel test model, there is a nonlinear dry friction damping arising from the rubbing or sliding between the experimental aeroelastic wing-fuselage model and the support spindle. This nonlinear factor is considered in the experimental–theoretical correlation study.

Extending the work by Dowell et al. (2003) and Tang et al. (2003), dynamic, transient conditions are considered in the present paper. A dynamic roll trim equation of motion of the wing-fuselage model with multiple control surfaces has been derived including aeroelastic effects and solved using a time marching technique. The capabilities of multiple control surfaces to effect roll maneuver transient response of the wing-fuselage model with a torsionally flexible wing are examined theoretically and experimentally. These results provide new insights into the dynamic behavior and design of an adaptive aeroelastic wing using trailing- and leading-edge control surfaces.

2. Experimental model and measurements

The experimental model consists of a right and left wing and a fuselage (slender body). For simplicity, the wing model is a rectangular aluminum plate of thickness 0.317 cm, total chord length (c) of 10.16 cm (including the leading and trailing control surface chords) and span length (l) of 10.16 cm. The plate has a very large bending and torsional stiffness and thus the wing per se is assumed to be rigid. The torsional flexibility of the wing is provided by a flat spring at the wing root which can be adjusted. The elastic axis is placed at the wing quarter chord. In order to place the chordwise center of gravity axis of the wing at the elastic axis as well, the leading-edge control surface is made of brass and the trailing-edge control surface is made of aluminum plate. Also a small slender body mounted at the wing root is used to provide weight balance. The leading and trailing control surfaces each have a chord length of 1.73 cm (17%c) and a full span length of 10.16 cm (100%l) hinged on the leading and trailing-edges, respectively. The rotation angle of each control surface can be adjusted.

The fuselage has a circular cross-section with a diameter of 2.54 cm. It includes two parts. The front part is a slender body with a parabolic forebody which can rotate about the fuselage center axis and supports the wings. The rear part is a nonrotating slender body with a parabolic aftbody which is used to support the front portion of the slender body and is connected to the wind tunnel floor by a support or sting rod. See Fig. 1.

The wings are allowed to rotate (roll) about the center axis of the fuselage. The start and stop mechanism for the rotation is provided by an electrical magnet brake. The transient rolling state (rolling angle) is measured by an Optical Shaft Encoder, E11, with 500 pulses per revolution mounted on the rear end of the nonrotating portion of the slender body. Every pulse corresponds to a certain rolling angle. But the time duration for one pulse may be changed during the experiment.

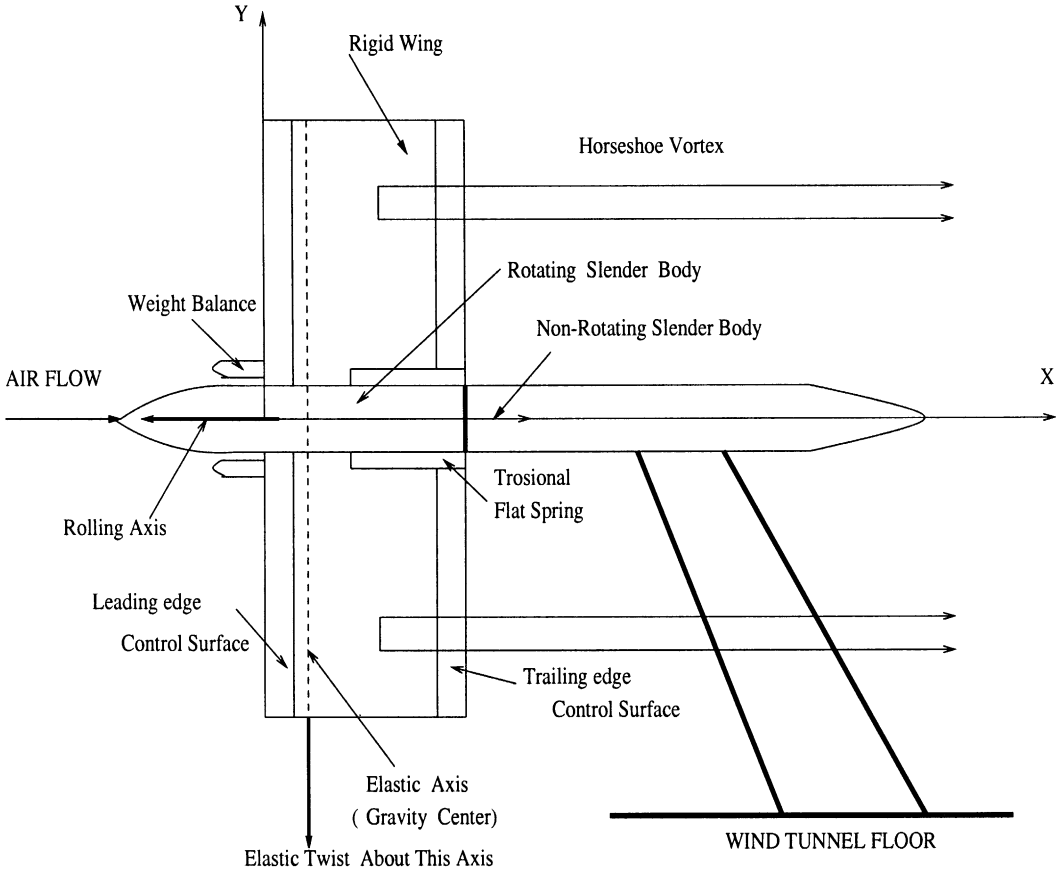

Fig. 1. Physical representation of experimental model. Also shown is a three-dimensional (linear) vortex lattice model of the unsteady flow.

Fig. 2. Photograph of the aeroelastic model in the wind tunnel.

Note that in the experimental testing protocol, the control surfaces are at a fixed rotation and the magnetic brake is used to prevent roll until a steady state aerodynamic field and aeroelastic deformation is achieved. Then, the brake is released and the rolling transient is observed and measured.

A physical representation of wing model geometry along with a three-dimensional vortex lattice model (linear) of the unsteady flow is shown in Fig. 1 and a photograph of the aeroelastic model in the wind tunnel is shown in Fig. 2.

3. Dynamic aeroelastic theoretical model

As shown in Fig. 1, a straight rectangular wing with leading- and trailing-edge control surfaces that are full span is considered. The theoretical/experimental model is symmetrical about the center axis of the fuselage. The aerodynamic forces on the fuselage (slender body) are neglected. The dynamic equation of torsional equilibrium about the elastic axis of the rigid wing expresses the balance of moments about the elastic axis due to the elastic spring and the aerodynamic forces in the Eulerian coordinate system (x, y, z):

$$I_\alpha \ddot{\alpha} + K_\alpha \alpha + M_y = 0 \tag{1}$$

or

$$I_\alpha \ddot{\alpha} + K_\alpha \alpha + \int_{r_f}^{l+r_f} \int_0^c \Delta p(x, y)(x - x_e)\, \mathrm{d}x\, \mathrm{d}y = 0, \tag{2}$$

where $\Delta p(x, y)$ is the pressure distribution on the wing, x_e is the distance from the elastic center to leading edge of the wing, I_α and K_α are the torsional inertia and stiffness, and α is the twist angle of the wing. r_f is the radius of the slender body (fuselage).

The rigid body dynamic rolling equation of equilibrium about the center axis of the fuselage is expressed as follows:

$$I_\phi \ddot{\phi} + M_d \frac{\phi}{|\phi|} - \int_{r_f}^{l+r_f} Ly \, \mathrm{d}y = 0 \tag{3}$$

or

$$I_\phi \ddot{\phi} + M_d \frac{\phi}{|\phi|} - \int_{r_f}^{l+r_f} y \int_0^c \Delta p(x,y) \, \mathrm{d}x \, \mathrm{d}y = 0. \tag{4}$$

In this equation a dry friction damping moment between the spindle support and the aeroelastic wing model is taken into account; I_ϕ is the rolling inertia and ϕ is the wing rolling angle; M_d is the nonlinear Coulomb friction damping moment coefficient.

Introducing nondimensional quantities into Eqs. (2) and (4) as follows:

$$\overline{\Delta p}(x,y) = \frac{\Delta p(x,y)}{\rho_\infty U^2}, \quad \bar{x} = \frac{x}{c}, \quad \bar{x}_e = \frac{x_e}{c}, \quad \bar{y} = \frac{y}{c}, \quad \bar{I}_\alpha = \frac{I_\alpha}{\rho_\infty U^2 c^3}, \quad \bar{I}_\phi = \frac{I_\phi}{\rho_\infty U^2 c^3},$$
$$\bar{K}_\alpha = \frac{K_\alpha}{\rho_\infty U^2 c^3} \quad \text{and} \quad \bar{M}_d = \frac{M_d}{\rho_\infty U^2 c^3},$$

the dimensionless equations corresponding to Eqs. (2) and (4) are

$$\bar{I}_\alpha \ddot{\alpha} + \bar{K}_\alpha \alpha + \int_{r_f/c}^{(l+r_f)/c} \int_0^1 \overline{\Delta p}(\bar{x},\bar{y})(\bar{x} - \bar{x}_e) \, \mathrm{d}\bar{x} \, \mathrm{d}\bar{y} = 0 \tag{5}$$

and

$$\bar{I}_\phi \ddot{\phi} + \bar{M}_d \frac{\phi}{|\phi|} - \int_{r_f/c}^{(l+r_f)/c} \bar{y} \int_0^1 \overline{\Delta p}(\bar{x},\bar{y}) \, \mathrm{d}\bar{x} \, \mathrm{d}\bar{y} = 0. \tag{6}$$

To model the above aeroelastic structural/fluid system, the aerodynamic flow about the structural model is assumed to be incompressible, inviscid and irrotational. Here an unsteady (linear) vortex lattice method is used to describe this flow. The wing and wake are divided into a number of elements. In the wake and on the wing all the elements are of equal size, Δx, in the streamwise direction. Point vortices are placed on the wing and in the wake at the quarter chord of the elements. At the three-quarter chord of each panel element a collocation point is placed for the downwash, i.e. the velocity induced by the discrete vortices is required to be equal to the downwash arising from the unsteady motion of the wing. Thus the following relationship is obtained:

$$w_i^{t+1} = \sum_j^{kmm} K_{ij} \Gamma_j^{t+1}, \quad i = 1, \ldots, km, \tag{7}$$

where w_i^{t+1} is the dimensionless downwash at the ith collocation point at time step $t+1$, Γ_j is the jth vortex strength normalized by cU, and K_{ij} is an aerodynamic kernel function for the horseshoe vortex. km and kmm are the number of vortex elements on the wing and total number of vortices on both the wing and wake in the x-direction, respectively. For the three-dimensional incompressible flow, the kernel function is given by

$$K_{ij}(\bar{x},\bar{y},\bar{x}_a,\bar{y}_a,\bar{x}_b,\bar{y}_b) = \frac{-1}{4\pi(\bar{y}_i - \bar{y}_{ja})}\left[1 + \frac{\sqrt{(\bar{x}_i - \bar{x}_{ja})^2 + (\bar{y}_i - \bar{y}_{ja})^2}}{\bar{x}_i - \bar{x}_{ja}}\right] + \frac{1}{4\pi(\bar{y}_i - \bar{y}_{jb})}\left[1 + \frac{\sqrt{(\bar{x}_i - \bar{x}_{ja})^2 + (\bar{y}_i - \bar{y}_{jb})^2}}{\bar{x}_i - \bar{x}_{ja}}\right], \tag{8}$$

where $\bar{x}_i$ is the location of the ith collocation point, and $\bar{y}_{ja}$ and $\bar{y}_{jb}$ are the locations of the two jth trailing vortex segments which are parallel to the x-axis at $\bar{y} = \bar{y}_a$ and $\bar{y} = \bar{y}_b$. See Section 10.4.7 (Horseshoe Vortex) of Katz and Plotkin (1991).

The aerodynamic matrix equation (general) is given by

$$[A]\{\Gamma\}^{t+1} + [B]\{\Gamma\}^t = [T]\{w\}^{t+1}, \tag{9}$$

where $[A]$ and $[B]$ are aerodynamic coefficient matrices. $[T]$ is a transfer matrix from the downwash on the local vortex lattice mesh on the wing to the global vortex lattice mesh. For the present model the wing span is finite and anti-symmetric about the center axis of the fuselage. An anti-symmetric vortex condition is used for reducing the aerodynamic degrees of freedom. In this case the aerodynamic coefficient matrix, $[A]$, corresponding to the kernel

function can be expressed as

$$A = K_{i,j}(\bar{x}, \bar{y}, \bar{x}_a, \bar{y}_a, \bar{x}_b, \bar{y}_b) - K_{i,j}(\bar{x}, \bar{y}, \bar{x}_b, -\bar{y}_b, \bar{x}_a, -\bar{y}_a).$$

The nondimensional downwash, w, contains contributions from the steady angle of attack α, the wing rolling rate, $p \equiv \mathrm{d}\phi/\mathrm{d}t$, and rotational angles, η_{le}, η_{te} of the leading and trailing control surfaces, respectively. For the present model, Eq. (9) is expressed in matrix form as

$$[A]\{\Gamma\}^{t+1} + [B]\{\Gamma\}^{t} = \{T_\alpha\}\alpha^{t+1} - \{T_p\}\frac{p}{U}^{t+1} + \{T_t\}\eta_{te} + \{T_l\}\eta_{le}, \tag{10}$$

where $\{T_\alpha\}$ and $\{T_p\}$ are the elastic twist and rolling rate transfer matrices for determining the relationship between the global vortex lattice mesh and the local vortex lattice mesh on the wing. $\{T_t\}$ and $\{T_l\}$ are the transfer matrices for determining the relationship between the global vortex lattice mesh and the local vortex lattice mesh on the trailing and leading control surfaces, respectively.

The nondimensional pressure distribution on the rigid wing at the jth point is given by

$$\overline{\Delta p_j} = \frac{c}{\Delta x}\left[(\Gamma_j^{t+1} + \Gamma_j^t)/2 + \sum_i^j (\Gamma_i^{t+1} - \Gamma_i^t)\right], \tag{11}$$

see Hall (1994).

Substituting Eq. (11) into Eq. (5) gives

$$\bar{I}_\alpha\ddot{\alpha} + \bar{K}_\alpha\alpha + \sum_{n=1}^{kn}\sum_{m=1}^{km}(\bar{x}_m - \bar{x}_e)[(\Gamma_{nm}^{t+1} + \Gamma_{nm}^t)/2 + \sum_i^m (\Gamma_{ni}^{t+1} - \Gamma_{ni}^t)]\Delta\bar{y} = 0 \tag{12}$$

or as expressed in matrix form,

$$\bar{I}_\alpha\ddot{\alpha} + \bar{K}_\alpha\alpha + \{D_2\}^{\mathrm{T}}\{\Gamma\}^{t+1} + \{D_1\}^{\mathrm{T}}\{\Gamma\}^{t} = 0, \tag{13}$$

where kn and km are the chordwise and spanwise numbers of vortex elements on the wing and here the superscript "T" indicates the matrix transpose.

Substituting Eq. (11) into Eq. (6) gives

$$\bar{I}_\phi\ddot{\phi} + \bar{M}_d\frac{\phi}{|\phi|} - \left\{\sum_{n=1}^{kn}\bar{y}_n\sum_{m=1}^{km}\left[(\Gamma_{nm}^{t+1} + \Gamma_{nm}^t)/2 + \sum_i^m (\Gamma_{ni}^{t+1} - \Gamma_{ni}^t)\right]\right\}\Delta\bar{y} = 0 \tag{14}$$

or as expressed in matrix form,

$$\bar{I}_\phi\ddot{\phi} + \bar{M}_d\frac{\phi}{|\phi|} - \{C_2\}^{\mathrm{T}}\{\Gamma\}^{t+1} - \{C_1\}^{\mathrm{T}}\{\Gamma\}^{t} = 0, \tag{15}$$

where D_1, D_2, C_1 and C_2 are coefficient matrices describing the vortex element forces and moments on the wing.

Thus, combining Eqs. (10), (13) and (15), a complete static aeroelastic state–space equation in matrix form is obtained for the unknown variables, Γ, α and ϕ,

$$\begin{bmatrix} A & 0 & T_p/U & -T_\alpha & 0 \\ D_2^{\mathrm{T}} & & & & \\ -C_2^{\mathrm{T}} & & [K_2] & & \\ 0 & & & & \\ 0 & & & & \end{bmatrix}\begin{Bmatrix}\Gamma\\ \dot{\alpha}\\ \dot{\phi}\\ \alpha\\ \phi\end{Bmatrix}^{t+1} + \begin{bmatrix} B & 0 & 0 & 0 & 0 \\ D_1^{\mathrm{T}} & & & & \\ -C_1^{\mathrm{T}} & & [K_1] & & \\ 0 & & & & \\ 0 & & & & \end{bmatrix}\begin{Bmatrix}\Gamma\\ \dot{\alpha}\\ \dot{\phi}\\ \alpha\\ \phi\end{Bmatrix}^{t} = \begin{Bmatrix} T_t\eta_{te} + T_l\eta_{le} \\ 0 \\ -\bar{M}_d\frac{\phi}{|\phi|} \\ 0 \\ 0 \end{Bmatrix}^{t+1/2}. \tag{16}$$

Following a similar treatment as described in Tang and Dowell (2001), a reduced-order aerodynamic model with static correction is constructed and the final aeroelastic state–space model is given by

$$\begin{bmatrix} I & -Y_{Ra}^{\mathrm{T}}[I - A(A+B)^{-1}]E \\ G_2X_{Ra} & K_2 + G_2(A+B)^{-1}E \end{bmatrix}\begin{Bmatrix}\gamma\\ \theta\end{Bmatrix}^{t+1} + \begin{bmatrix} -Z_{Ra} & Y_{Ra}^{\mathrm{T}}B(A+B)^{-1}E \\ G_1X_{Ra} & K_1 + G_1(A+B)^{-1}E \end{bmatrix}\begin{Bmatrix}\gamma\\ \theta\end{Bmatrix}^{t}$$
$$= \begin{Bmatrix} 0 \\ -(G_1+G_2)(A+B)^{-1}(T_t\eta_{te} + T_l\eta_{le}) + F_N \end{Bmatrix}^{t+1/2}, \tag{17}$$

where $\{\theta\} = \{\dot{\alpha}, \dot{\phi}, \alpha, \phi\}^{\mathrm{T}}$ is a vector of unknown variables and

$$[E] = [0, \{-T_p/U\}, \{T_\alpha\}, 0], \quad [G_2] = \begin{bmatrix} \{D_2\}^{\mathrm{T}} \\ -\{C_2\}^{\mathrm{T}} \\ 0 \\ 0 \end{bmatrix}, \quad [G_1] = \begin{bmatrix} \{D_1\}^{\mathrm{T}} \\ -\{C_1\}^{\mathrm{T}} \\ 0 \\ 0 \end{bmatrix}, \quad [K_2] = \begin{bmatrix} \bar{I}_\alpha/\Delta t & 0 & \bar{K}_\alpha/2 & 0 \\ 0 & \bar{I}_\phi/\Delta t & 0 & 0 \\ -1/2 & 0 & 1/\Delta t & 0 \\ 0 & -1/2 & 0 & 1/\Delta t \end{bmatrix},$$

$$[K_1] = \begin{bmatrix} -\bar{I}_\alpha/\Delta t & 0 & \bar{K}_\alpha/2 & 0 \\ 0 & -\bar{I}_\phi/\Delta t & 0 & 0 \\ -1/2 & 0 & -1/\Delta t & 0 \\ 0 & -1/2 & 0 & -1/\Delta t \end{bmatrix}, \quad \{F_N\} = \begin{Bmatrix} 0 \\ -\bar{M}_d \frac{\phi}{|\phi|} \\ 0 \\ 0 \end{Bmatrix}, \tag{18}$$

$[X_{Ra}]$, $[Y_{Ra}]$ are the reduced right and left eigenvector matrices of the vortex lattice aerodynamic model and $[Z_{Ra}]$ is a reduced aerodynamic eigenvalue matrix, $\Gamma = X_{Ra}\gamma$, with only the most dominant eigenmodes retained in the analysis.

4. Numerical study

A standard discrete time marching algorithm has been used to calculate the dynamic response of this aeroelastic system using the full aerodynamic model, Eq. (16), and also the reduced-order aerodynamic model, Eq. (17). The time step is constant for a given flow velocity U, $\Delta t = \Delta x/U$. For these calculations, the parameters of an experimental model studied here and in Tang et al. (2003) are used. The measured torsional and rolling inertia moments are $I_\alpha = 8.22 \times 10^{-6}$ kg m s^2 and $I_\phi = 8.95 \times 10^{-5}$ kg m s^2 for $r = 0$ or $I_\phi = 8.78 \times 10^{-5}$ kg m s^2 for $r = 1$ or $r = -1$, respectively. The leading-edge device for $r = 0$ is (slightly) different from that for $r = \pm 1$ hence the difference in values for I_ϕ. The measured torsional stiffness is $K_\alpha = 0.032$ kg m/rad. The trailing-edge control surface rotation is $\eta_{te} = 5^\circ$. Two typical cases for leading-edge control are considered, i.e. the ratios of leading- to trailing-edge control surface rotations are $r = 0$ and 1. The measured dry friction damping moment between the spindle support and the aeroelastic wind tunnel model is $M_d = 0.00021$ kg m.

Consider now the present three-dimensional flow model for the wing. The wing was modelled using 400 vortex elements, i.e. $km = 40$, $kn = 10$. The wake was modelled using 800 vortex elements, i.e. $kmm = 120$. The total number of vortex elements (or aerodynamic dof) was 1200. The aerodynamic eigenmodes are extracted from this model and a small number, $R_a = 11$, are used in the aeroelastic analysis. A convergence study has shown that $R_a = 11$ is sufficient to give good accuracy.

Fig. 3(a) shows the transient response of rolling rate, p, for $U = 25$ m/s, $r = 1$ and $M_d = 0$. (Note that $p \equiv \dot{\phi}$.) The initial conditions for ϕ and α are zero. There are three curves in this figure for three distinct cases. When both torsional and rolling inertia moments are considered the response is indicated by the broken line. This is a rising oscillatory curve. The aeroelastic oscillatory frequency is near the torsional natural frequency $\omega_\alpha = 10$ Hz. (Note that the oscillatory frequency varies with the flow velocity.) When only the rolling inertia is considered and the torsional inertia neglected, ($I_\alpha = 0$), the response is indicated by the solid line. This is similar to a unit-step response of a first-order system. One of the important characteristics of this response is an exponential response function and convergence to a steady value. For reference, the static rolling rate for both $I_\alpha = 0$ and $I_\phi = 0$ is shown by the dashed-point line. Fig. 3(b) shows the transient response of the rolling angle, ϕ. The response is almost the same with and without torsional inertia included as

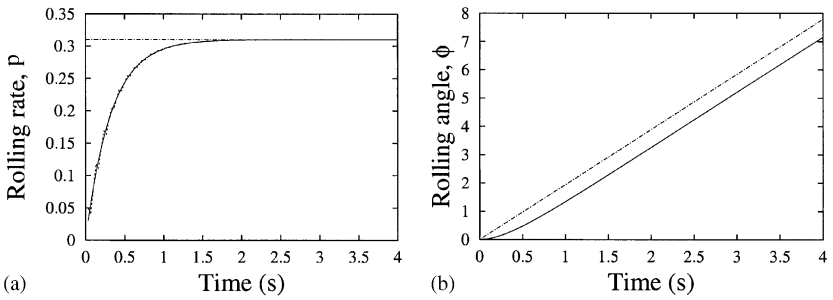

Fig. 3. Transient response for $U = 25$ m/s and $r = 1$: (a) rolling rate, and (b) rolling angle.

shown by the broken and solid lines. There is a difference between the dynamic and static response for the rolling angle and this difference is constant when the steady state is reached. The value of the rolling angle is dependent on the rolling inertia and system damping. The rolling rate for both the transient dynamic and static or steady state response is the same when the steady state is reached.

Examining the solid line curve of the Fig. 3, the transient response of this system can be described approximately by an exponential function, i.e.

$$p(t) = p_s(1 - e^{-\xi t}) \quad (t \geqslant 0), \tag{19}$$

where p_s is a static rolling rate and ξ is a damping coefficient.

A curve fitting method is used to determined the damping coefficient from data such as that shown in Fig. 3. Fig. 4 shows a typical transient response time history and the corresponding fitted data for $U = 15$ m/s, $r = 1$ and $M_d = 0$. The time history and static rolling rate (steady value) are indicated by the solid line. The fitted data is indicated by the symbol of ○. From these data a settling time, t_s can be defined. The settling time is the time required for the response curve to reach within a certain range of the steady (static) value, say within 5%. This 5% tolerance criterion may be useful for studies of rolling rate control. For the present conditions, t_s is 1.7 s as indicated by a dashed-point line.

Fig. 5 shows the transient response of the rolling rate for three flow velocities $U = 15$, 27 and 30 m/s for $r = 1$, $I_\alpha = 0$. The solid line is for the case of $M_d = 0$ and the broken line is for the case of $M_d = 0.00021$ kg m. For $U = 15$ and 30 m/s, the initial rolling rate is zero and the transient responses have the expected exponential response behavior. The rolling rate with dry friction damping is smaller than that without dry friction damping. For $U = 27$ m/s, the initial rolling rate is set to 1 Hz, thus a difference between with and without dry friction damping cases can be more readily seen. At this velocity, the steady rolling rate is $p = 0$ with dry friction damping included. In this case, the response does not have an exponential response behavior.

Figs. 6(a) and (b) show the system damping, ξ, and settling time, t_s, versus flow velocity for $r = 1$, $I_\alpha = 0$. The solid line with the points, ○, is for the case of $M_d = 0$ and the broken line with the points, △, is for the case of $M_d =$ 0.00021 kg m. The results are obtained using a data fitting method. As shown in Fig. 6(a), for the case of $M_d =$ 0.00021 kg m, there are some missing points for $U < 7.5$ m/s and 25 m/s $< U <$ 28 m/s, because in these ranges the steady rolling rates are zero due to the effects of dry friction. The damping increases as the flow velocity increases and the damping is almost independent of dry friction damping over most, but not all, of the flow velocity range. This means the system damping, ξ, is generally dominated by the aerodynamic damping. As shown in Fig. 6(b), the settling time, t_s, decreases as the flow velocity increases.

Similar results are obtained for $r = 0$ as will be shown later. It is interesting to note that the system damping, ξ, and settling time, t_s, are very close to those for $r = 1$, i.e. the effects of r on the aerodynamic damping and t_s are very small.

Now consider the rigid wing case, i.e. the torsional stiffness is infinite, $K_\alpha = \infty$. Fig. 7 shows the transient response of the rolling rate for two typical flow velocities $U = 6$, 18 m/s, $r = 1$ and $I_\alpha = 0$. The solid line is for the case of $M_d = 0$ and the broken line is for the case of $M_d = 0.00021$ kg m. For $U = 18$ m/s, the initial rolling rate is zero and the transient responses have a exponential response behavior. The rolling rate with dry friction damping is smaller than that without dry friction damping. For $U = 6$ m/s, the initial rolling rate is set to 1 Hz and the transient response of the rolling rate with dry friction damping approaches zero when $t > 2.7$ s. It does not have an exponential response

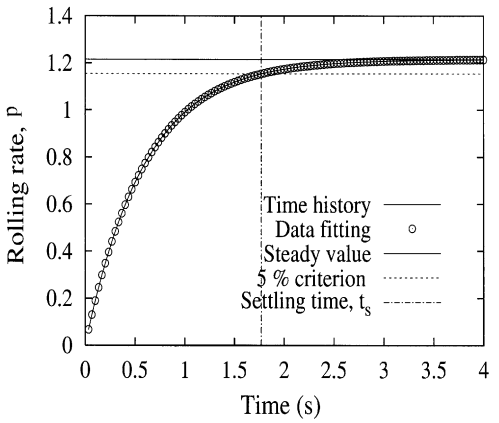

Fig. 4. Transient response time history and corresponding the fitted data for $U = 15$ m/s and $r = 1$.

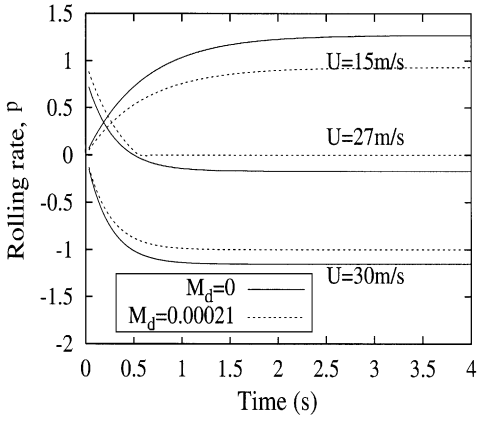

Fig. 5. Transient response curves for $U = 15$, 27, 30 m/s and $r = 1$.

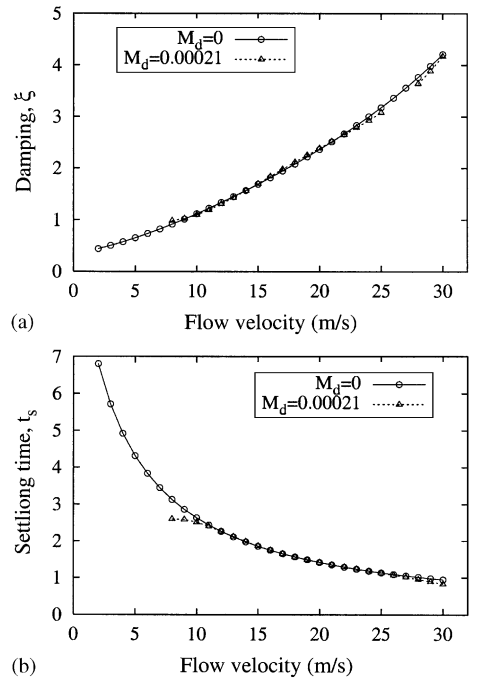

Fig. 6. System damping, ξ, and settling time, t_s, versus flow velocity for $r = 1$: (a) system damping, and (b) settling time.

behavior. Figs. 8(a) and (b) show the system damping, ξ, and settling time, t_s, versus flow velocity for $r = 1$, $I_\alpha = 0$. The lines and symbols have the same meaning as in Fig. 6. The results are similar to those for the torsionally elastic case, but the damping values are different. Structural torsional stiffness has a larger effect on the aerodynamic damping than the ratio of control surface rotation angles, r.

Fig. 9(a) shows the transient response when increasing or decreasing flow velocity. The calculation model is a torsional elastic system with only the rolling inertia moment included for $r = 1$ and $M_d = 0.00021$ kg m. The solid line is for increasing flow velocity and the broken line is for decreasing flow velocity. There are eight flow velocities considered in the calculation from $U = 9$ to 30 m/s with $\Delta U = 3$ m/s when flow velocity is increasing and $U = 27$–6 m/s with $\Delta U = 3$ m/s when it is decreasing. The calculation starts from the increasing flow velocity case with zero initial rolling rate. At each flow velocity, the computation is for 4 s. The computational time step, Δt, is $1/2048$ s. The

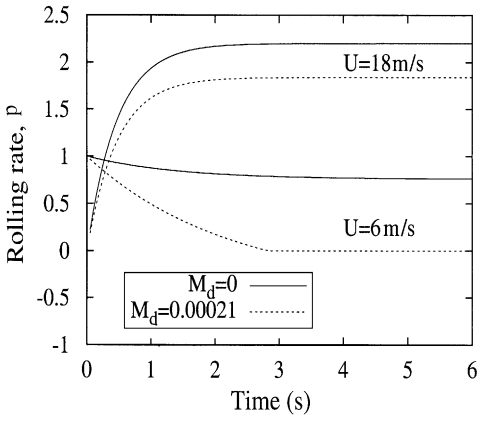

Fig. 7. Transient response curves for the rigid case for $U = 6$, 18 m/s and $r = 1$.

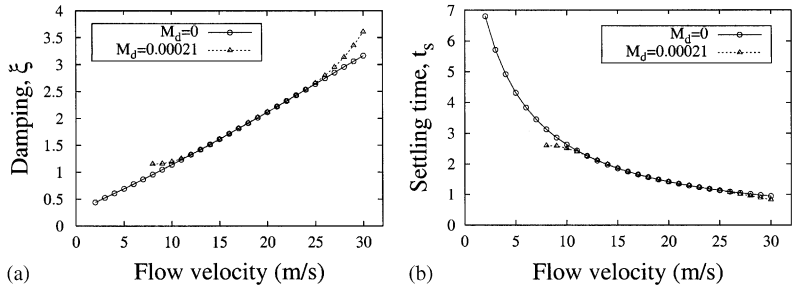

Fig. 8. System damping, ξ and settling time, t_s versus flow velocity for the rigid case and $r = 1$: (a) system damping, and (b) settling time.

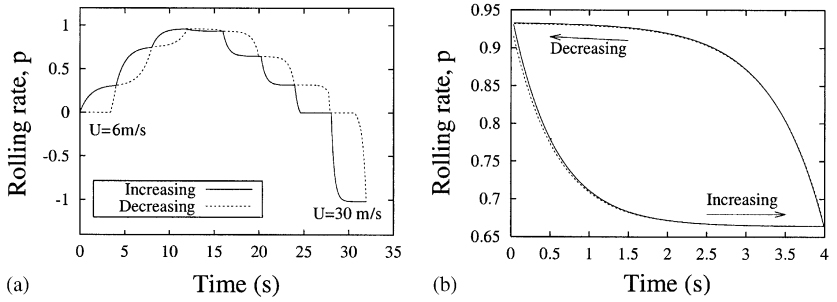

Fig. 9. Transient time history for rolling rate for increasing and decreasing flow velocities. $r = 1$ and $M_d = 0.00021$ kg m: (a) continuous transient history, and (b) typical transient history.

transient response is shown in time intervals of 4 s for each flow velocity increment. For the next flow velocity (increasing ΔU), initial conditions are provided by the previous transient response state. This process is continuous in time until the flow velocity increases to $U = 30$ m/s. For the decreasing velocity process, initial conditions are provided by the last transient response of $U = 30$ m/s to calculate the transient response of $U = 27$ m/s. This process is continuous in time until the flow velocity decreases to $U = 6$ m/s.

Fig. 9(b) shows a typical transient response for the increasing and decreasing flow velocity cases from $U = 18$ to 21 m/s and from $U = 21$ to 18 m/s, respectively. The solid line is the result from the time history and the broken line is the result from a data fitting. The system damping is $\xi = 1.7$ for $U = 21$ m/s and the increasing velocity case, and $\xi = 1.4$ for $U = 18$ m/s and the decreasing velocity case.

Corresponding to Fig. 9, Figs. 10(a) and (b) show the system damping, ξ, and settling time, t_s, versus flow velocity. The symbol, $\bigcirc$, is the result from the increasing flow velocity process and the symbol, $\triangle$, is the result from the decreasing flow velocity process. Note that at $U = 6$ and 27 m/s, one cannot calculate the damping value, ξ, using the present data fitting method because of the discontinuous change in slope of the rolling rate as a function of time due to dry friction effects. See Fig. 7. The two results from the increasing and decreasing flow velocity cases are very close. No detectable hysteresis phenomenon was found from the theoretical model, even though the effects of dry friction damping are included.

5. Theoretical and experimental correlation

For the present computational and experimental model, the aerodynamic and structural parameters are described in the previous section, "Experimental Model and Measurements". The trailing-edge control surface rotation is $\eta_{te} = 5^\circ$. Two typical cases are considered in the experiment, i.e. the ratios of leading- to trailing-edge control surface rotations are $r = 0$ and 1.

From the experiment measurement, a time series of 500 pulses is obtained as shown in Fig. 11. $t_0, t_1, \ldots, t_i, \ldots, t_n$ in the figure are the time sequence. Thus, the rolling angle at t_1 is $2\pi/500$ rad and at t_i, the rolling angle is represented as

$$\phi = i\frac{2\pi}{500}. \tag{20}$$

As an example, Fig. 12(a) shows the measured data from Encoder transducer, E11, for $U = 14.83$ m/s for the case of $r = 1$ and the flexible wing. Because the measured data do not provide an exact square wave, an average pulse voltage is calculated as shown by the dashed line of Fig. 12(a). The pulse time sequence t_i is then determined using an intersection

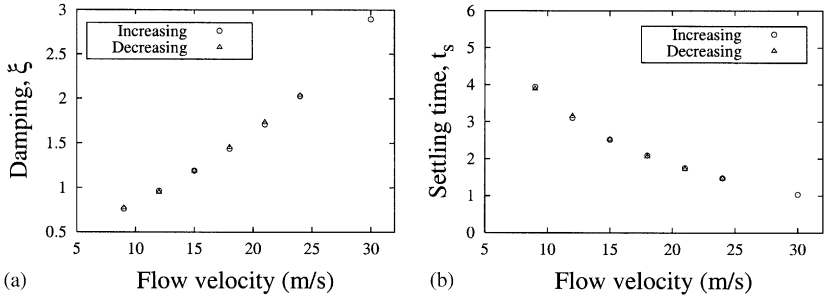

Fig. 10. System damping, ξ, and settling time, t_s, versus flow velocity for $r = 1$, $M_d = 0.00021$ kg m and $K_z = 0.032$ kg m/rad: (a) system damping, and (b) settling time.

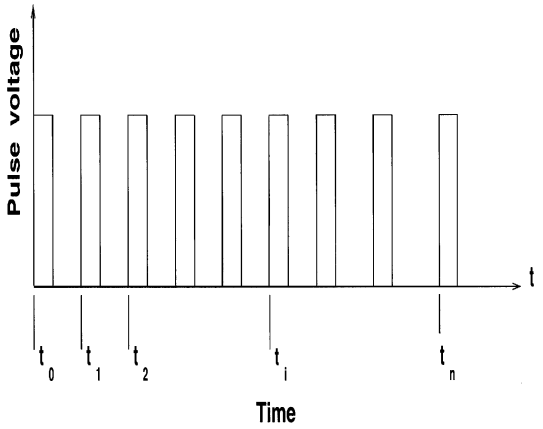

Fig. 11. Diagram for pulses obtained from Encoder, E11.

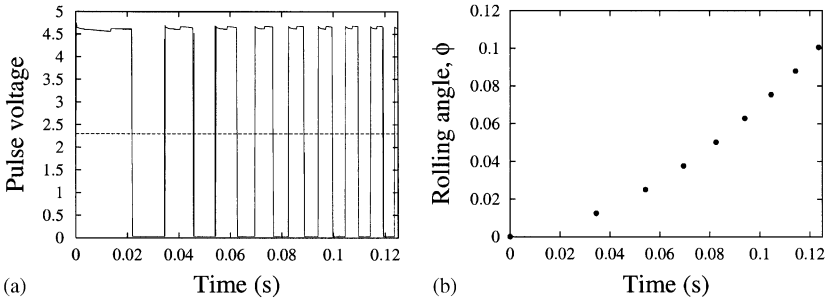

Fig. 12. Pulses and corresponding rolling angle for $U = 14.83$ m/s and $r = 1$: (a) pulses, and (b) rolling angle.

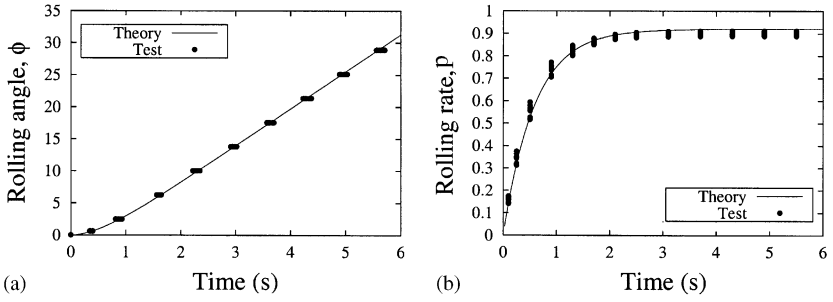

Fig. 13. Transient response for $U = 14.83$ m/s and $r = 1$: (a) rolling angle, and (b) rolling rate.

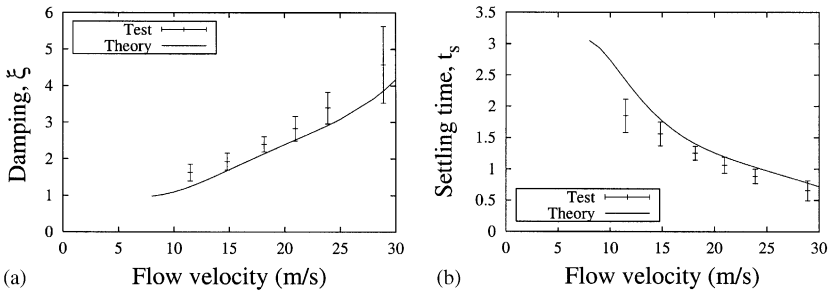

Fig. 14. System damping, ξ, and settling time, t_s, versus flow velocity for $r = 1$: (a) system damping, and (b) settling time.

point of the ith pulse with the average line. The corresponding rolling angle can be determined using Eq. (20). The results are shown in Fig. 12(b).

A curve fitting method is then used to determine the damping coefficient, ξ, and the steady rolling rate, P. This method is similar to that used in the theoretical analysis. The transient rolling rate is determined by a numerical differentiation method from the measured rolling angle data.

Fig. 13 shows the transient response history and a comparison of theory with experiment for $U = 14.83$ m/s for the case of $r = 1$ and the flexible wing. The solid line shows the results from theoretical analysis and the symbols, •, are the results obtained from the experiment. The experiment is repeated over 10 times. All the experimental results are shown in Fig. 13. Fig. 13(a) shows the transient response of rolling angle, ϕ. Note that for a particular rolling angle, the pulse time is slightly different for each test run. Fig. 13(b) shows the transient response for the rolling rate, p. Theoretical and experimental results are in good agreement.

Because the damping coefficient, ξ, is very sensitive to the measurement error, 10 tests for each case are used in the present measurement. The mean value and error tolerance of the damping coefficient are then calculated. Figs. 14(a) and (b) show the system damping, ξ, and settling time, t_s, versus flow velocity for $r = 1$ and the flexible wing. The solid

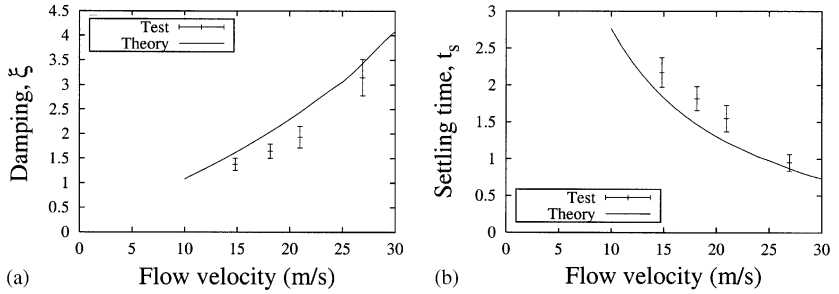

Fig. 15. System damping, ξ, and settling time, t_s, versus flow velocity for $r = 0$: (a) system damping, and (b) settling time.

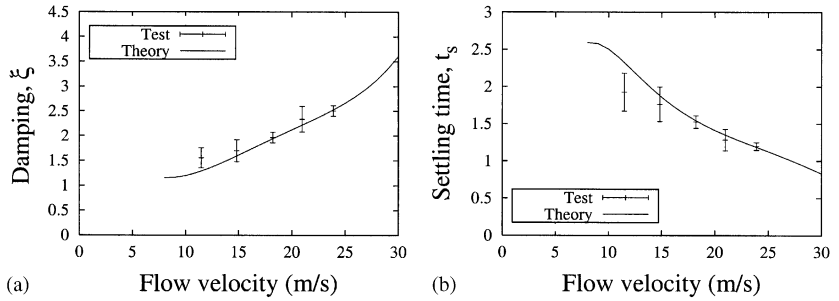

Fig. 16. System damping, ξ, and settling time, t_s, versus flow velocity for the rigid case and $r = 1$: (a) system damping, and (b) settling time.

line shows the theoretical results and the bars show the experiment data including measurement uncertainty. The agreement between theory and experiment is reasonably good.

Similar results are obtained for $r = 0$ as shown in Fig. 15. The line and symbols shown in this figure are the same as for Fig. 14.

Fig. 16 shows the transient response for $r = 1$ and the rigid wing. The solid line indicates the theoretical results and the dashed line is for experimental data. The agreement is again good.

6. Concluding remarks

An experimental/theoretical correlation study of a rolling aeroelastic wing with leading- and trailing-edge control surfaces has been carried out. Good correlation between theory and experiment is shown for the transient and steady state response of the system. The transient behavior shows no unusual or unexpected anomalies suggesting that state-of-the-art theoretical methods for transient as well as steady state rolling may be used with confidence for analysis and design.

Acknowledgements

This work was supported by DARPA through AFOSR Grant F49620-99-1-00253, "Aeroelastic Leveraging and Control Through Adaptive Structures", under the direction of Dr Ephrahim Garcia and Dr Dan Segalman. Dr Robert Clark is the Duke University Principal Investigator. All numerical calculations were done on a supercomputer, T916, in the North Carolina Supercomputing Center (NCSC).

References

Andersen, G., Forster, E., Kolonay, R., Eastep, F., 1997. Multiple control surface utilization in active aeroelastic wing technology. Journal of Aircraft 34, 552–557.

Ardilean, E., Clark, R.L., 2001. V-stack piezoelectric actuator, SPIE Eighth Annual International Symposium on Smart Structures and Materials, 4–8 March, Newport Beach, CA, USA.

Dowell, E.H., Hall, K.C., 2001. Modeling of fluid–structure interaction. Annual Review of Fluid Mechanics 33, 445–490.

Dowell, E.H., Bliss, D.B., Clark, R.L., 2003. An adaptive aeroelastic wing with leading and trailing edge control surfaces. Journal of Aircraft 40, 559–565.

Flick, P.M., Love, M.H., 1999. The impact of active aeroelastic wing technology on conceptual aircraft design. Paper Presented at the RTO AVT Specialists Meeting on Structural Aspects of Flexible Aircraft Control, Ottawa, Canada, October 18–20, RTO MP-36.

Hall, K.C., 1994. Eigenanalysis of unsteady flows about airfoils, cascades, and wings. AIAA Journal 32, 2426–2433.

Katz, J., Plotkin, A., 1991. Low-speed Aerodynamics. McGraw-Hill, New York.

Noll, T.E., Eastep, F.E., 1995. Active flexible wing program. Journal of Aircraft 32, 9.

Prechtl, E.F., Hall, S.R., 1999. Design of a high efficiency, large stroke, electromechanical actuator. Journal of Smart Materials and Structures 8 (1), 13–30.

Tang, D.M., Dowell, E.H., 2001. Effects of angle of attack on nonlinear flutter of a delta wing. AIAA Journal 39, 15–21.

Tang, D.M., Aiqin Li, Dowell, E.H., 2003. Experimental and theoretical study on rolling effectiveness of multiple control surfaces. AIAA Journal 41, 160–167.

Weisshaar, T.A., Duke, D.K., Dobbins, A., 2000. Active aeroelastic tailoring with adaptive continuous control surfaces. AIAA Paper 2000-1619.

Yurkovich, R.R., 1995. Optimum wing shape for an active flexible wing. Proceedings of the AIAA/ASME/ASCE/ARS 36th Structures, Structural Dynamics and Materials Conference, New Orleans, LA, USA.

Zink, P.S., Mavris, D.N., Love, M.H., Karpel, M., 1998. Robust design for aeroelastically tailored/active aeroelastic wing. Seventh AIAA/USAF/NASA/SSMO Symposium on Multidisciplinary Analysis and Optimization, St. Louis, MO, September 2–4, AIAA Paper 98-4781.